

Carbon/Cr₂O₃ nanocrystal Composites as an Anode with Improved Lithium Storage Performance

Yongtao Li^{1,2,3}, Yuzhou Liu¹, Chenyong Shi², Xiuqian Liang², Liqing Liu^{1,3,*}, Hongguang Zhang^{1,3}, Xuemin He^{1,3} and Yanwen Ma⁴

¹ College of Science, Nanjing University of Posts and Telecommunications, Nanjing 210023, P. R. China.

² College of Electronic Science and Engineering, Nanjing University of Posts and Telecommunications, Nanjing 210023 P. R. China.

³ New Energy Technology Engineering Laboratory of Jiangsu Province, Nanjing University of Posts and Telecommunications, Nanjing 210023, P. R. China.

⁴ College of material science and Engineering, Nanjing University of Posts and Telecommunications, Nanjing 210023 P. R. China.

*E-mail: liulq@njupt.edu.cn

Received: 5 November 2021 / Accepted: 22 December 2021 / Published: 2 February 2022

Carbon-coated Cr₂O₃ composites were prepared by the hydrothermal reaction of ammonium chromate ((NH₄)₂CrO₄) and sucrose to form a polymer that was then annealed and carbonized at 600°C under an argon atmosphere to generate nanoparticles of the anodic nanocomposites. The results of electrochemical test showed that the nanocomposite with 49.0 wt% carbon content has more stable and excellent electrochemical performance as the anode material for lithium-ion batteries. The diameters of the Cr₂O₃ crystals in the nanocomposites were 20-50 nm, which helped to modulate the volume expansion of Cr₂O₃ crystals beneath the external carbon shell and ultimately greatly improved the lithium storage performance and discharge/charge (i.e. lithiation/delithiation) cycling stability of the nanocomposites. The specific capacity of the nanocomposite with carbon content of 49.0 wt% was 542 mAh·g⁻¹ after 300 cycles, which was significantly higher than the capacity of the bare Cr₂O₃ crystals. In addition, as the cycle number increased, the specific capacity of the battery also steadily increased. These results indicated that the composite material is a promising candidate as an anode material for lithium-ion batteries.

Keywords: Carbon-coated; Lithium storage performance; Lithium-ion batteries;

1. INTRODUCTION

Lithium-ion batteries (LIBs) have become a mainstay in the energy storage market because they contain fewer toxic, expensive metals than other batteries, which makes them more environmentally

friendly and more inexpensive. Therefore, lithium-ion batteries have become an integral source of energy in nearly every sector and industry that rely on batteries. Currently, conventional carbon batteries, including lithium-ion batteries, are gradually limiting the development of many electronic products, such as portable communication devices and electric vehicles, due to their low specific capacity ($372 \text{ mAh}\cdot\text{g}^{-1}$) [1-4]. Therefore, researchers have focused on developing new anode materials to improve the energy density of lithium-ion batteries. Co_3O_4 , Fe_2O_3 , MnO , NiO , and other transition metal-containing oxides all have high theoretical specific capacities. In particular, Cr_2O_3 is considered a promising anode material for LIBs because of its high theoretical specific capacity ($1058 \text{ mAh}\cdot\text{g}^{-1}$) and low discharge platform, both of which are higher than other transition metal oxides [5].

Much like other transition metal oxides, Cr_2O_3 undergoes a dramatic change in volume upon Li^+ embedding, which results in damage to the internal structure of the material and, therefore, in a rapid decline in battery performance as the number of discharge/charge cycles increases. This problem severely limits the application of this material in LIBs. It was previously discovered that these problems could be effectively resolved by replacing the bare electrode material with carbon-coated nanocrystals featuring a core-shell structure [6-9]. For example, Zhou et al. synthesized $\text{Cr}_2\text{O}_3@\text{C}$ composites in one step using an explosive reaction, which enhanced the Li^+ storage performance [10]. This method was straightforward, and the synthesis of the composite material was trivial; however, the composite demonstrated a specific capacity of only $397 \text{ mAh}\cdot\text{g}^{-1}$ after 50 cycles at a current density of $119 \text{ mA}\cdot\text{g}^{-1}$. Guo et al. prepared a mesoporous carbon- Cr_2O_3 composite by sintering, whose structured material maintained a specific capacity of $639 \text{ mAh}\cdot\text{g}^{-1}$ after 80 cycles at a current density of $50 \text{ mA}\cdot\text{g}^{-1}$ [11].

To circumvent the issues that previous researchers have encountered with composite anode materials, we used ammonium chromate ($(\text{NH}_4)_2\text{CrO}_4$) as a precursor to synthesize the anode material of LIBs. In a reactor, $(\text{NH}_4)_2\text{CrO}_4$ was hydrothermally reacted with sucrose (carbon source), resulting in the formation of nanocomposite particles with a very stable core-shell structure. The micro- and nanostructure of the core-shell had larger specific surface areas compared to the bare Cr_2O_3 crystals, which enabled the material to efficiently modulate the expansion of the volume of the electrode material while charging/discharging and effectively guarantee the stability of the structure, while the carbon material further enhanced the electrical conductivity of the electrode. As a result, the multiplier performance and cycle stability of Li-ion batteries improved compared to the bare Cr_2O_3 crystals [12-14]. The hydrothermal reaction reduced the heavy, toxic, hexavalent chromium (Cr(VI)) species into less-toxic, trivalent chromium (Cr(III)) without the concomitant production of toxic gas. The whole reaction process is not only easy to synthesize, but also reduces the amount of pollution generated [15-18]. Overall, the electrochemical performance of the $\text{Cr}_2\text{O}_3@\text{C}$ composite was greatly improved compared with the bare Cr_2O_3 anode material.

2. EXPERIMENTAL

2.1 Synthesis of $\text{Cr}_2\text{O}_3@\text{C}$

The $\text{Cr}_2\text{O}_3@\text{C}$ composite was prepared by hydrothermal synthesis by reacting ammonium chromate with sucrose in a reactor. First, pellets of ammonium chromate pellets (1.521 g) and sucrose

(1.708 g and 3.416 g to prepare molar ratios of 2:1 and 1:1, respectively) were added to a beaker and dissolved in deionized water to prepare a 60 mL solution. The solution was magnetically stirred vigorously for 30 min at 600 rpm, followed by 30 min of ultrasonic shaking. The solution was then transferred to a 100 mL Teflon-lined stainless steel autoclave and heated at 160°C for 20 h. After the reactor cooled to room temperature, the resulting precipitate was repeatedly washed with deionized water for filtration. The gray-green precipitate was cured in a blast drying oven at 80°C for 12 h. The samples were then heated to 600°C under an argon atmosphere at a heating rate of 3°C/min; after reaching 600°C, the temperature was maintained for 3 h. For comparison, the naked Cr₂O₃ was prepared by sintering ammonium chromate crystals under the same conditions. In this paper, the composite samples with molar ratios of ammonium chromate to sucrose of 2:1 and 1:1 were labeled as A₁ and A₂, respectively, and the bare Cr₂O₃ sample was labeled as B.

2.2 Characterization

2.2.1 Material Characterization

The crystalline phases of A₁, A₂, and B were determined by powder X-ray diffraction (XRD, Rigaku Ultima IV, Tokyo, Japan) with a scan angle (2θ) from 10° to 80°. The microscopic morphologies of the samples were characterized by scanning electron microscopy (SEM, FEI Quanta FEG650, Hillsboro, OR, USA) and transmission electron microscopy (TEM). Raman spectra were obtained using a laser Raman spectrometer (Raman, Horiba) at an excitation wavelength of 630 nm to elucidate the degree of graphitization and sp²-hybridized bond structure of the carbon material within the Cr₂O₃@C composite. In addition, thermogravimetric analysis (TGA) was used to determine the thermal stabilities of the anodic materials.

2.2.2 Electrochemical measurements

The working electrode was prepared by mixing calcined active material, carbon black (Super-P), and *N*-methylpyrrolidone (NMP) in a 70:20:10 ratio (by weight) and then coating thick copper foil with the mixture. Pure lithium foil was used as counter electrode. The electrolyte consisted of a 1 M solution of LiPF₆ in a mixture of diethyl carbonate (EC), dimethyl carbonate (DMC) and ethyl carbonate (EMC) (1:1:1, v/v). Celgard 2500 polypropylene was used as a spacer. Discharge-charge measurements were performed in a cell cycler (NEWARE-CT4008) with a voltage range of 0.01-3 V at current densities of 100, 200, 500, 1000, and 2000 (mA·g⁻¹). Cyclic voltammetry (CV) measurements were performed by a Correst electrochemical workstation over a potential window of 0.01-3 V (vs Li/Li⁺) at a scan rate of 0.1 mV·s⁻¹. Electrochemical impedance spectroscopy (EIS) measurements were also performed in this workstation over the frequency range of 100 kHz-0.01 Hz. All measurements were performed at room temperature.

3. RESULTS AND DISCUSSION

3.1 Morphologies and microstructures of the $\text{Cr}_2\text{O}_3@\text{C}$ nanocomposite electrodes

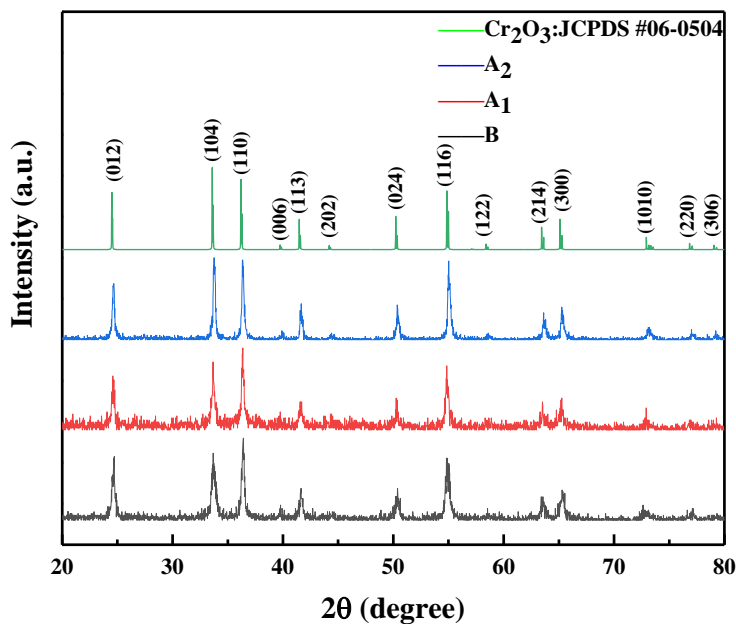


Figure 1. XRD patterns of the $\text{Cr}_2\text{O}_3@\text{C}$ nanocomposites with different carbon contents and bare Cr_2O_3 powder.

Fig. 1 displays the XRD spectra of the three samples, A_1 , A_2 , and B, using the standard card of Cr_2O_3 (JCPDS #06-0504) for comparison. The diffraction patterns of the electrode materials A_1 , A_2 , and B were all highly consistent with the XRD spectrum of the standard Cr_2O_3 crystals. In addition, no diffraction peaks corresponding to elemental Cr or other Cr oxides were detected in the spectra of A_1 , A_2 , and B. The multiple sharp peaks in the spectra indicated that the samples had a high crystallinity of the Cr_2O_3 phase.

Raman spectroscopy was used to further investigate the degree of graphitization of the carbon material within the A_1 and A_2 nanocomposite samples. The Raman spectra of the two samples featured two peaks with strong absorptions at 1358 cm^{-1} and 1556 cm^{-1} , which corresponded to the conventional D and G bands (Fig. 2). The presence of the D band was evidence of low graphitization of carbon in the composites, while the G band was representative of the sp^2 -hybridized structure of the carbon atoms in the composites [19]. The intensity ratios (I_D/I_G) of the A_1 and A_2 samples were 1.05 and 1.03, respectively; higher intensity ratios indicated that there were more irregularities and defects on the surface of the composite [20, 21]. The higher the degree of this defect, the more conducive to the conduction of electrons, which were favorable for facilitating conductivity and increasing the Coulombic efficiency of the materials.

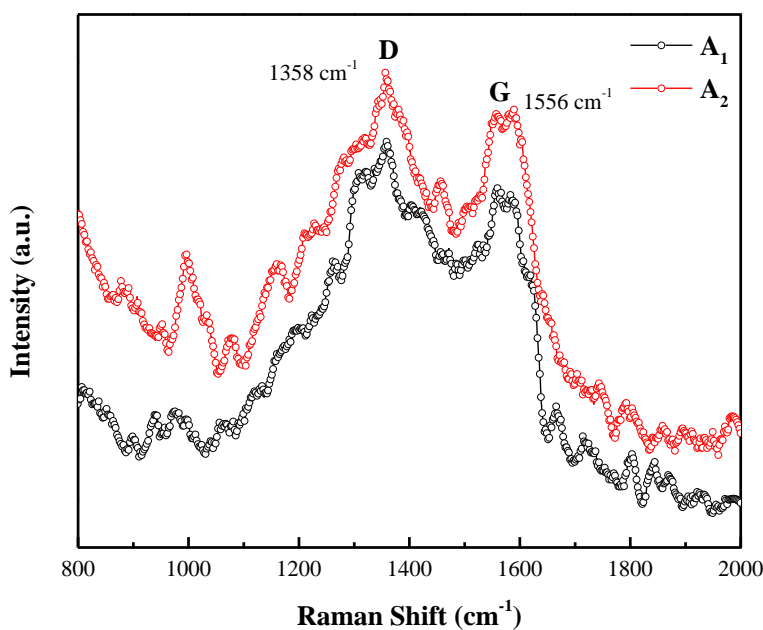


Figure 2. Raman spectra of the Cr₂O₃@C nanocomposites with different carbon contents.

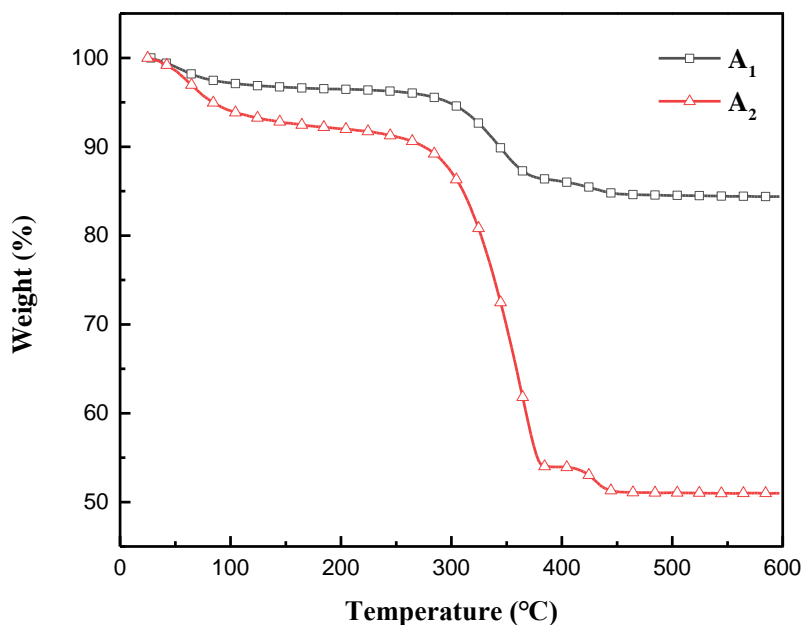


Figure 3. TGA curves of the Cr₂O₃@C nanocomposites with different carbon contents.

Thermogravimetric analysis (TGA) was used to determine the carbon content in the two Cr₂O₃@C nanocomposites, and the experiments were performed under an air atmosphere. As shown in Fig. 3, the A₁ and A₂ samples were heated. Based on the amount of residual material after thermal

decomposition to x °C, it was determined that the A₁ and A₂ nanocomposites contained 15.6% and 49.0% carbon by mass, respectively.

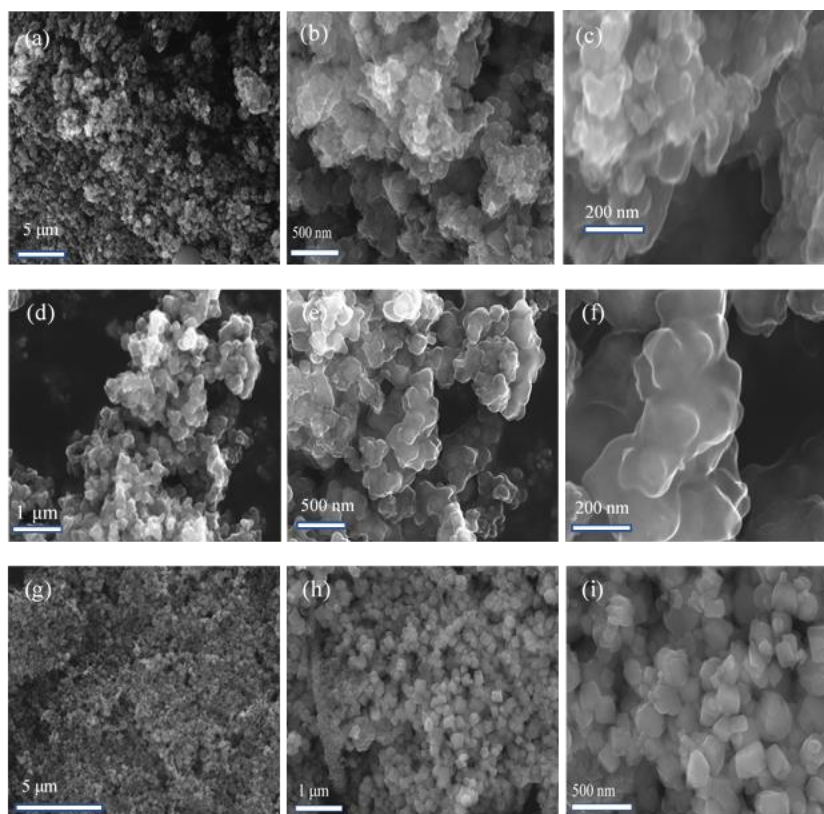


Figure 4. SEM images of Cr₂O₃@C-A₁ (a), (b), (c); SEM images of Cr₂O₃@C-A₂ (d), (e), (f); SEM images of Cr₂O₃-B (g), (h), (i) at different magnifications.

The microscopic morphologies of the nanocomposite electrode materials with different carbon contents were observed by SEM (Fig. 4a-c) In the images, the exposed Cr₂O₃ nanoparticles consisted of a cubic morphology and featured an overly aggregated distribution. In addition, the nanoparticles did not demonstrate a uniform size distribution, as there were many nanoparticles with very large diameters (100-200 nm) ; these large nanoparticles were detrimental to the discharge/charge cycling stability of the battery cell. The morphology of composite A₁ is shown in Fig. 4d, 4e, and 4f at 1 μm, 500 nm, and 200 nm resolutions, respectively. The nanoparticles of A₁ were small and spherical in morphology, and they had a uniform size distribution. In addition, the translucent carbon shell with a white inner core was easily observed in the magnified image (Fig.4e, 4f), which was consistent with the core-shell structure mentioned previously. The SEM images of composite A₂ are shown in Fig. 4g, 4h, and 4i. The nanoparticles of A₂ were more optimized compared to A₁, which means they were interconnected and wrapped together, such that no individual carbonaceous particles were observed.

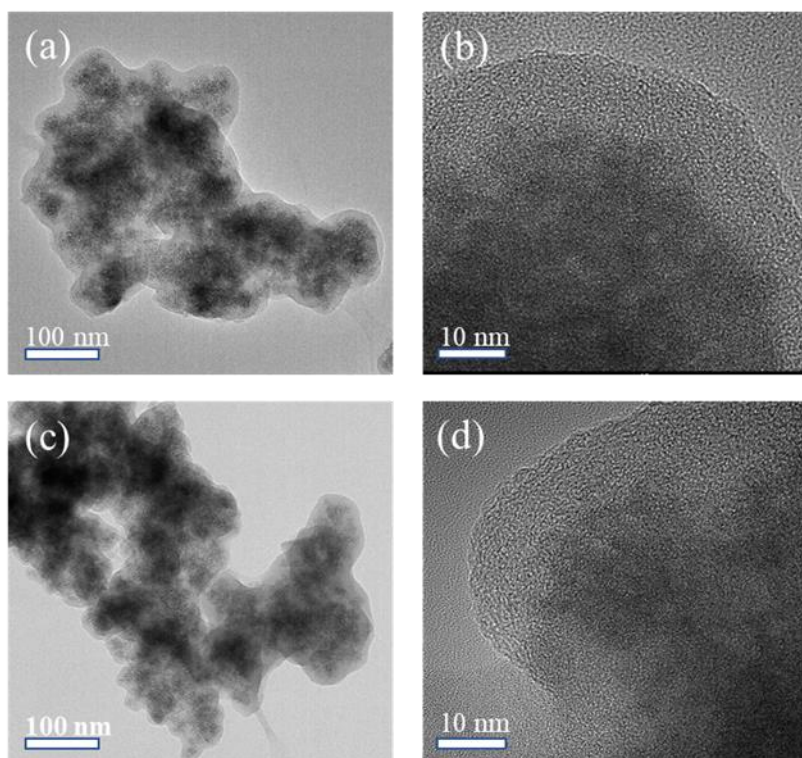


Figure 5. TEM images of Cr₂O₃@C-A₁ (a) and (b) at different magnifications; SEM images of Cr₂O₃@C-A₂ (c) and (d) at different magnifications.

The microscopic morphologies of the two Cr₂O₃@C composites were further characterized by TEM (Fig. 5). The Cr₂O₃@C composites consisted of black Cr₂O₃ crystalline particles with diameters between 20-50 nm that were completely encapsulated by a translucent carbon shell, forming a stable structure. These morphologies were more apparent in the HRTEM images of the composites (Fig 5b and 5d for the A₁ and A₂ composites, respectively); as the carbon content of the composite Cr₂O₃@C increased, the amorphous carbon shell became thicker, more deeply covering the Cr₂O₃ crystals. This core-shell structure functioned to relieve any changes in the volume of the Cr₂O₃ crystals and prevent the particles from crushing during battery cycling, which ultimately improved the battery cycling performance [22].

3.2 Electrochemical properties of Cr₂O₃@C nanocomposite electrodes

Fig. 6a and 6b display the CV curves of the Cr₂O₃@C nanocomposite electrodes in the voltage range of 0.01-3.0 V at a scan rate of 0.1 mV·s⁻¹. A distinct, broad reduction peak near 0.86 V appeared in the first cycle of the cathodic scan, but the peak nearly disappeared in the two subsequent cycles. This reduction peak corresponded to the formation of a solid electrolyte interphase (SEI) layer due to the decomposition of the solid electrolyte on the active material [23, 24]. In the anodic scan, a sharp oxidation peak was observed near 1.44 V, which also disappeared in the subsequent cycles; the disappearance of this peak could have been the result of side reactions between the electrolyte and the electrode [25]. The charging/discharging curves of A₁, A₂, and B at a current density of 100 mA·h⁻¹·g⁻¹ are

displayed in Fig. 6c, 6d, and 6e. The specific capacities of the first discharge of A₁, A₂, and B were 1434 mAh·g⁻¹, 1279 mAh·g⁻¹, and 968 mAh·g⁻¹, respectively.

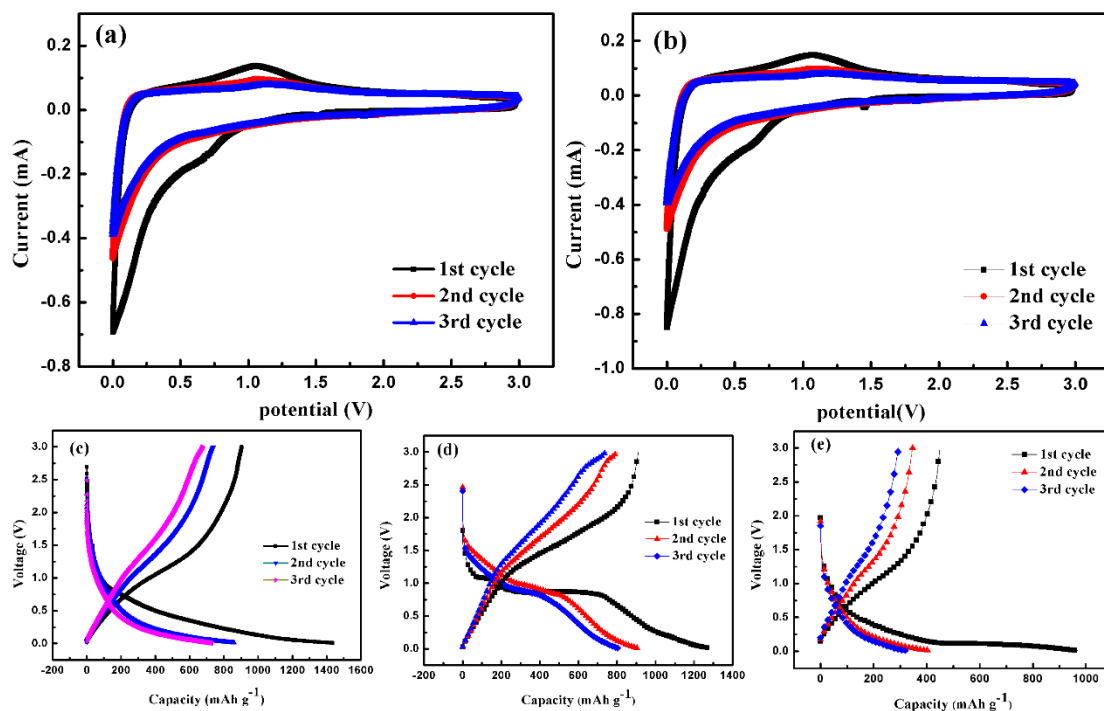
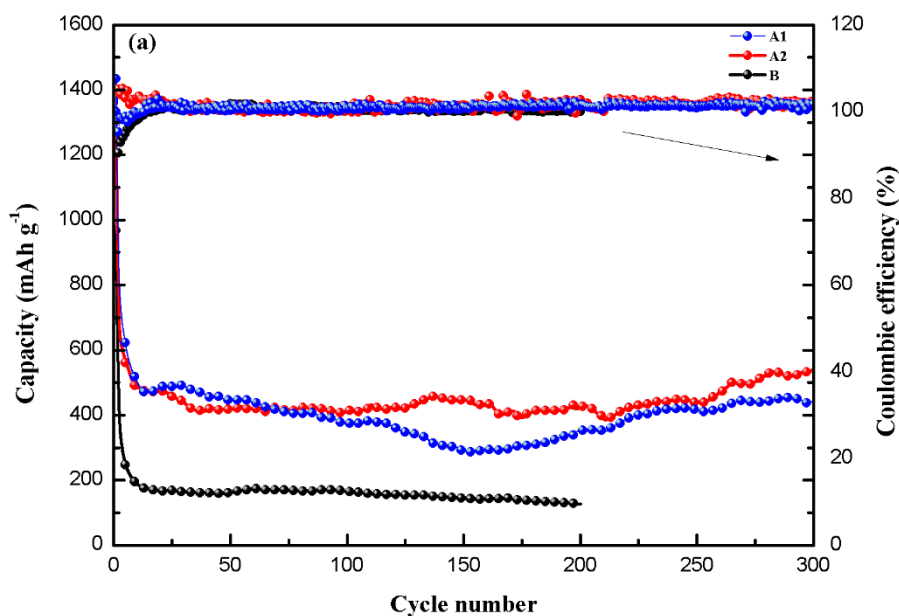


Figure 6. CV profiles of Cr₂O₃@C-A₁ (a); Cr₂O₃@C-A₂ (b) in the 0.01-3.0 V voltage window; charge/discharge curves of Cr₂O₃@C-A₁ (c), Cr₂O₃@C-A₂ (d), and Cr₂O₃-B (e) at a current density of 100 mA·g⁻¹.

The differences in the specific capacities of the initial discharge between the three samples was attributed to the varying carbon contents of the samples.



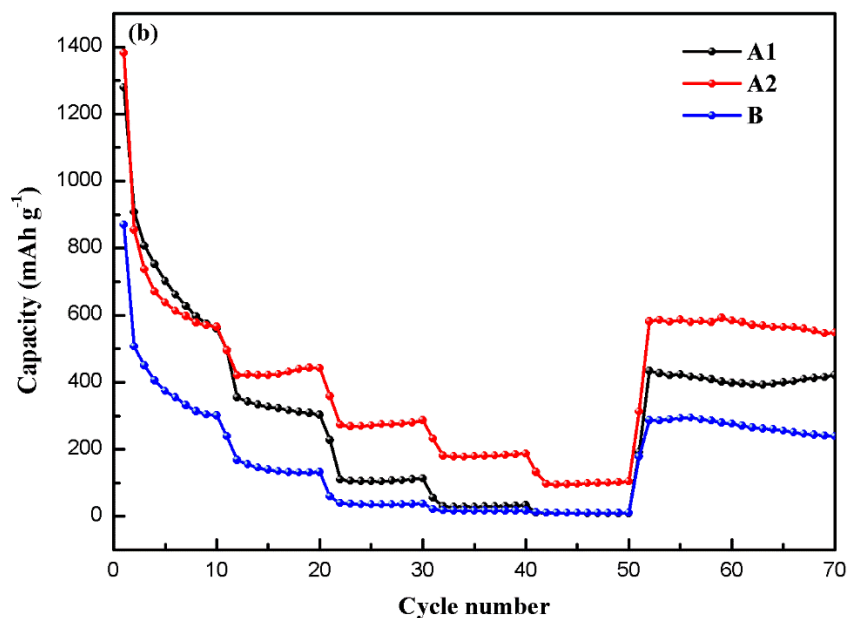


Figure 7. Cycling performance and coulombic efficiency of the different electrode samples after several discharge/charge cycles performed at a current density of $100 \text{ mA} \cdot \text{g}^{-1}$ (a); (b) rate capability of the different electrode samples at different current densities.

In the second discharge/charge cycle, the specific capacities of all three samples decreased by a certain fraction due to the formation of an SEI film layer. The irreversible capacity of samples A₁ and A₂ decreased by 37.02% and 29.08%, respectively, both of which were much lower than the 53.51% calculated for the bare Cr₂O₃ crystals (sample B). This substantial difference indicated that the presence of the amorphous carbon shells was extremely effective in enabling the retention of the specific capacity of the cells.

Figure. 7a shows the long-term discharge/charge cycle performance of the three samples at a current density of $100 \text{ mA} \cdot \text{g}^{-1}$. The coulombic efficiency of all three nanomaterials quickly reaches 100% or higher (due to the sufficient lithium content of the negative electrode of the half-cell, lithium removal/intercalation situation occurs, resulting in a coulombic efficiency $>100\%$). The specific capacity gradually leveled off after 20 cycles, but the bare Cr₂O₃ electrode (sample B) had a specific capacity of only 126 mAh g^{-1} after 200 charge/discharge cycles. On the other hand, the specific cell capacities of samples A₁ and A₂ were consistently much higher than those of sample B. The battery capacity decayed faster under the first few cycles and then leveled off. However, after about 150 cycles, the battery specific capacity of sample A₁ and sample A₂ started to show a small trend of increasing. Finally, after the 300th cycle, the specific capacities of sample A₁ and sample A₂ increased to 442 mAh g^{-1} and 542 mAh g^{-1} , respectively. As shown in Table 1, we compare this result with the results of the two documents mentioned in the introduction, and we can find that it is more valuable. This electrochemical test performed more cycles while taking into account the appropriate current density, and finally reached a satisfactory result.

Table 1. Comparison with the reference mentioned in the introduction

Composite material	Current density	Cycle number	Cycle performance	Reference
Carbon encapsulated Cr ₂ O ₃	119 mA g ⁻¹	50	397 mAh g ⁻¹	Zhou [10]
Mesoporous carbon-Cr ₂ O ₃	50 mA g ⁻¹	80	639 mAh g ⁻¹	Guo [11]
Carbon/Cr ₂ O ₃	100 mA g ⁻¹	300	542 mAh g ⁻¹	This work

This decrease and then a small increase in the specific capacity of the cells is common in such composites. In combination with the structure of the composites, the increase in capacity may be due to several reasons. First, the core-shell structure has stabilized during the long cycle of the cell, but some components of the SEI film will provide some cell specific capacity during the reversible electrocatalytic conversion reaction. Second, the interface between metal nanoparticles and amorphous Li₂O can provide an environment for lithium insertion, which we often mention as interfacial Li-storage.

As shown in Fig. 7b, despite the gradual decline in the capacity in the first 50 discharge/charge cycles, the capacity of composite A₂ recovered to 581 mAh·g⁻¹ after 50 cycles at current densities of 100 mA·g⁻¹, 200 mA·g⁻¹, 500 mA·g⁻¹, 1000 mA·g⁻¹, and 2000 mA·g⁻¹. In particular, A₂ was still able to produce a stable specific capacity even at high current densities, which might have been attributed to the thicker amorphous carbon layer that allowed for expansion of the nanomaterial, thereby effectively avoiding the crushing and destruction of the nanoparticles [26, 27]. This result indicated that composite A₂ could easily retain capacity even after cycling at different current densities, in addition to its long-term electrochemical cycling stability. It should be emphasized that the carbon-cladding strategy significantly enhanced the specific capacity, cycling stability and multiplicative performance of the nanocomposite cell compared to the bare Cr₂O₃ crystals. Moreover, the nanocomposite cell with lower carbon content (A₁) was not capable of effectively sustaining the changes in the internal volume, as well as a stable conductive architecture, during lithiation/delithiation. Given these results, more nanocomposites with different molar ratios of the carbon material to Cr₂O₃ should be prepared to determine the effect of the different ratios on the specific capacity of the cell in hopes that higher specific capacities can be achieved.

4. CONCLUSION

Cr₂O₃@C composites were successfully synthesized under hydrothermal method by using sucrose as carbon source. The Cr₂O₃@C composites consistently outperformed the bare Cr₂O₃ crystals in terms of cell performance. The leap in cell performance is mainly attributed to the formation of a robust core-shell structure in the composites. These 20 nm-50 nm diameter crystals are encapsulated in

an amorphous carbon shell, which limits the growth of Cr₂O₃ crystals even at high cell cycling temperatures and greatly enhances the lithium storage performance. The steadily increasing specific capacity of the battery also provides room for more far-reaching research on this material.

ACKNOWLEDGMENTS

This work is financially supported by National Natural Science Foundation of China under contracts No.51772157 and by the research project of Nanjing University of Posts and Telecommunications under contract Nos. NY217096 and NY211144.

References

1. J. Liu, Z.N. Bao, Y. Cui, E.J. Dufek, J.B. Goodenough, P. Khalifah, Q. Li, B.Y. Liaw, P. Liu and A. Mathiram, *Nat. Energy*, 4 (2019) 180.
2. Z.Y. Wu, J. Luo, P. Jiao, H. Liu, B.B. Chang and X.Y. Wang, *Green. Energy. Environ.*, 6 (2021) 517.
3. C.P. Yang, L. Zhang, B.Y. Liu, S.M. Xu, T. Hamann, D. McOwen, J.Q. Dai, W. Luo, Y.H. Gong and E.D. Wachsman, *P. Natl. Acad. Sci. USA*, 115 (2018) 3770.
4. H.M. Sun, L.M. Wang, D.Q. Chu, Z.C. Ma and A.X. Wang, *Mater. Lett.*, 140 (2015) 158.
5. A.S. Hameed, M.V. Reddy, B.V.R. Chowdari and J. Vittal, *RSC. Adv.*, 4 (2014) 64142.
6. B.B. Wu, S.Y. Wang, W.J. Evans, D.Z. Deng, J.H. Yang and J. Xiao, *J. Mater. Chem. A.*, 4 (2016) 15266.
7. S. Gao, N. Wang, S. Li, D. Li, Z. Cui, G. Yue, J. Liu, X. Zhao, L. Jiang and Y. Zhao, *Angew. Chem. Int. Edit.*, 132 (2020) 2486.
8. W.J. Li, Y.N. Zhou and Z.W. Fu, *Appl. Surf. Sci.*, 257 (2011) 2881.
9. Y. Zhang and C.D. Wang, *Mater. Today. Energy*, 16 (2020) 100406.
10. Y. Zhou, B.Y. Liu, Y.F. Shao, C.H. Fan, R.H. Fan and B.S. Wen, *Funct. Mater. Lett.*, 11 (2018) 1.
11. B.K. Guo, M.F. Chi, X.G. Sun and S. Dai, *J. Power. Sources*, 205 (2012) 495.
12. L. Dupont, S. Laruelle, S. Grugeon, C. Dickinson, W. Zhou and J.M. Tarascon, *Journal. Power. Sources*, 175 (2008) 502.
13. Y. Xiang, Z. Chen, C.M. Chen, T.H. Wang and M. Zhang, *J. Alloy. Compd.*, 724 (2017) 406.
14. B. Yang, S. Zhou, J. Zeng, L.P. Zhang, R.H. Zhang and K. Liang, *Nano. Res.*, 13 (2020) 1013.
15. N. Yu, L.X. Zou, C. Li and K. Guo, *Appl. Surf. Sci.*, 483 (2019) 85.
16. Y. Zhao, Y. Li, C.L. Ma and Z.P. Shao, *Electrochimica Acta*, 213 (2016) 98.
17. Z.Q. Cao, M.L. Qin, B.R. Jia, L. Zhang, Q. Wan, M.S. Wang, A.A. Volinsky and X.H. Qu, *Electrochimica Acta*, 139 (2014) 76.
18. X. Li, K.J. Zhang, M. David, Z.Z. Yang, M.S. Wang, Y. Tang, F.Jiang, Y.G. Du and J.M. Zheng, *Chem. Mater.*, 30 (2018) 2566.
19. K. Wang, S.E. Pei, Z.S. He, L.A. Huang, S.S. Zhu, J.F. Guo, H.B. Shao and J.M. Wang, *Chem. Eng. J.*, 356 (2018) 272.
20. M.J. Zachman, Z.Y. Tu., S. Choudhury, L.A. Archer and L.F. Kourkoutis, *Nature*, 560 (2018) 345.
21. Z. Wang, D. Luan, S. Madhavi, Y. Hu and X.W. Lou, *Energ. Environ. Sci.*, 5 (2012) 5252.
22. Y. Liu, H. Kang, L. Jiao, C. Chen, K. Cao, Y. Wang and H. Yuan, *Nanoscale*, 7 (2015) 1325.
23. B. K. Guo, X.Q. Wang, P.F. Fulvio, M.F. Chi, S.M. Mahurin, X.G. Sun and S. Dai, *Adv. Mater.*, 23 (2011) 4661.
24. J.S. Liang, F.L. Huo, Z.Y. Zhang, W.F. Yang, M. Javid, Y. Jung, X.L. Dong and G.Z. Cao, *Appl. Surf. Sci.*, 476 (2019) 1000.
25. M.K. Kim, W.H. Shin and H.M. Jeong, *Appl. Surf. Sci.*, 467 (2019) 926.

26. J.F. Qian, W.A. Henderson, W. XU, P. Bhattacharya, M. Engelhard, O. Borodin and J.G. Zhang, *Nat. Commun.*, 6 (2015) 1518.
27. L.Z. Long, S.J. Wang, M. Xiao and Y.Z. Meng, *J. Mater. Chem. A.*, 4 (2016) 10038.

© 2022 The Authors. Published by ESG (www.electrochemsci.org). This article is an open access article distributed under the terms and conditions of the Creative Commons Attribution license (<http://creativecommons.org/licenses/by/4.0/>).